How does surface integrity of nanostructured surfaces induced by severe plastic deformation influence fatigue behaviors of Al alloys with enhanced precipitation?

Pierre Maurel, Laurent Weiss, Thierry Grosdidier, Philippe Bocher

How does surface integrity of nanostructured surfaces induced by severe plastic deformation influence fatigue behaviors of Al alloys with enhanced precipitation?

Pierre Maurel[a,b,c,*], Laurent Weiss[a], Thierry Grosdidier[a,c,**], Philippe Bocher[b,**]

[a] *Université de Lorraine, Laboratoire LEM 3, UMR CNRS 7239, 7 Rue Félix Savart, 57073 Metz, France*
[b] *Laboratoire d'Optimisation des Procédés de Fabrication Avancés (LOPFA), École de Technologie Supérieure, 1100 rue Notre-Dame Ouest, Montréal, QC H3C 1K3, Canada*
[c] *LABoratoire d'EXcellence "Design of Alloy Metals for low-mAss Structures" (LABEX-DAMAS), 7 rue Félix Savart, 57073 Metz, France*

Abstract

Effects on fatigue behaviors and microstructures of Surface Mechanical Attrition Treatment (SMAT) before or after precipitation aging have been investigated on two hardenable Al alloys.

The aluminum alloy with high notch sensitivity (7075) should not be processed by SMAT as the generated low surface integrity is always detrimental to fatigue performances. On less notch sensitive alloys (2024), SMAT before aging formed smaller and denser precipitates, resulting in a high hardened depth, and microstructures more resistant to residual stress relaxation than after conventional shot-peening. SMAT after aging resulted in a significant improvement of fatigue performance with only subsurface crack nucleation sites.

Keywords: Severe Plastic Deformation (SPD), Aluminium, High Cycle Fatigue, Surface Mechanical Attrition Treatment (SMAT), Precipitation aging, Duplex treatment

Highlights

- Effects of SMAT after precipitation aging or aging after SMAT treatment were studied

*Corresponding author.
**Secondary corresponding authors.
Email addresses: pierre.maurel@univ-lorraine.fr (Pierre Maurel), thierry.grosdidier@univ-lorraine.fr (Thierry Grosdidier), philippe.bocher@etsmtl.ca (Philippe Bocher)

- Aging after SMAT displayed denser and finer precipitates with deeper hardness in 2024
- Aging after SMAT showed higher relaxation resistance than conventional shot-peening
- Due to high notch sensitivity, 7075 always displayed low fatigue resistance after SMAT
- 2024 had a significant fatigue resistance increase after SMAT

1. Introduction

Severe plastic deformation (SPD) treatments allowed the development of materials with impressive mechanical properties. As reviewed in several papers [1–3], studies pointed that the induced microstructure refinements and high dislocation densities could significantly increase hardness, strength, fatigue resistance, wear resistance as well as, in some cases, the corrosion resistance. However, this usually comes at the cost of a lower ductility. Unfortunately, most SPD processes, such as High-Pressure Torsion [4] or Equal Channel Angular Pressure [5], require considerable amount of load or are restricted to deform relatively small samples with simple geometries. Thus, up-scaling such processes to industrial applications remains extremely difficult.

Because the external surface of industrial parts is generally the most solicited one (higher load, friction, corrosion), focusing on reinforcing the surfaces appears as a viable and easier way to gain the added value of these refined structures. To this end, several severe plastic deformation techniques have been developed such as Laser Shock Peening [6], Burnishing [7], Surface Mechanical Attrition Treatment (SMAT) [8–12] or Ultrasonic Shot Peening (USP or USSP) [13]. These two last processes consist in propelling a media (usually metallic balls between 1 mm and 10 mm in diameter) on the sample surface to deform it and produce a microstructural refinement. These surface SPD techniques introduce high compressive residual stress at the surface [11] similarly to conventional shot-peening [9, 14–16], the technique from which SMAT has been developed. In addition, given enough time, the severe plastic deformation of the surface generates surface microstructure refinement as

well as microstructure and property gradients along the depth. Since both, compressive residual stresses and finer microstructures, are known to retard crack propagation [14], an improvement on the fatigue resistance could be expected. Although, fatigue resistance improvement was reported after SMAT by several authors, other authors have reported a decrease of the fatigue properties due to the influence of the peening energy on the roughness and surface integrity, as pointed in review papers [9, 12]. Additionally, Mutoh et al. exposed important fold-like defects which shortened the crack initiation lives for peened specimens due to stress concentration [17]. Those fold-like defects cannot be detected with roughness measurements.

The combination of thermal treatments with SPD treatments on specific materials and microstructures is an interesting approach allowing the modifications of microstructural transformations and mechanical characteristics [18–25]. For example, several authors have published works about combining SPD processes with precipitation aging in aluminium (2000 and 7000 series) [20, 22–25]. It was observed that the high deformation produced a high dislocation density and a finer microstructure which increased the numbers of nucleation sites where precipitates could nucleate. This resulted in an ultrafine and more homogeneous precipitation [20, 23]. Mechanical tests revealed strengths higher than those obtained on the same material only deformed by rolling [20]. Interestingly, not only the strength was improved, a high ductility was also obtained [20, 24]. As previously discussed, ductility is generally severely impaired after SPD processes. Thus the combination of SPD and heat treatment could be an interesting issue on Al alloys. This has never been tested in the case of surface treatment, to the knowledge of the authors. This is surprising as it is well established that surface thermo-mechanical treatments are also an interesting issue for surface processing. For example, Novelli et al. [18, 19] determined that SMAT at cryogenic temperature enhanced the martensitic transformation and further improved subsurface hardness in metastable austenitic stainless steel compared to SMAT at room temperature. SMAT is mainly advertised for its fatigue resistance improvement, thus it appears as a sensible test to characterize the combination effectiveness for industrial applications [26].

The fatigue resistance of SMATed surfaces has already been investigated for the 7075

aluminium alloys [13]. However, the impact of SMAT on the precipitation aging and its subsequent effect on fatigue properties has yet to be studied. Several papers studied the thermal stability of the nanostructures obtained by SMAT on pure aluminium [27, 28]. They revealed that the grain size remained sub-micrometric for temperatures as high as 200 °C. The idea of combining SMAT with other treatments has already received some attention in other applications. For example, the corrosion resistance of the Microarc Oxidation Process (MAO) performed on 2024 nanostructured surface by SMAT was investigated and showed encouraging results in some conditions [29].

The high residual stress gradient introduced by SMAT in the subsurface layer is one of the main reasons of the improved fatigue resistance. However, using an aging would relax this residual stress. A competition should then appear in terms of fatigue resistance between the relaxation effect and the microstructure obtained from the combined SMAT and Aging treatment. Additionally, the impact of SMAT on surface integrity should affect the fatigue resistance.

In this context, this paper investigates two main axes.

(i) The impact of the surface integrity after SMAT on the fatigue resistance: samples from two aluminium alloys with different notch sensitivities [30, 31] were SMATed and a comparison to as-machined and as-polished samples is proposed.

(ii) The impact of the order of thermo-mechanical treatments on the fatigue resistance: aged then SMATed and SMATed then aged samples are compared.

2. Methodology

2.1. Materials and treatments

Two common industrial aluminium alloys, the 2024 and the 7075, were bought from Tacinas and Est Aciers Industrie S.A.S. respectively. The chemical composition of the 2024 was [wt%]: Si 0.1, Fe 0.16, Cu 4.3, Mn 0.7, Mg 1.3, Ti 0.1, Al (balance). The chemical composition of the 7075 was [wt%]: Si 0.1, Fe 0.44, Cu 1.42, Mn 0.02, Mg 2.74, Cr 0.24, Zn 6.07, Al (balance).

Both alloys came in the form of extruded bars with a diameter of 20 mm and 12 mm respectively for the 2024 and 7075 alloys. The bars were machined into cylindrical fatigue samples such as the one shown in Fig. 1. The L direction is the extrusion direction of the bars. Major $\langle 111 \rangle$ and minor $\langle 100 \rangle$ fibre textures are known to develop along the extrusion direction in aluminium alloys [32].

For the Surface Mechanical Attrition Treatment (SMAT), as illustrated in Fig. 1, the samples (red) were positioned horizontally with the bottom part of the 6 mm diameter section at a distance of 20 mm from the vibrating device (blue). The vibrating device was bought from SONATS [26] and was set at 20 kHz for a 60 μm amplitude. The samples rotated at a constant speed of 20 rpm. The media, 2 mm in diameter AISI 52100 steel balls, was confined in the treatment chamber (green) and occupied roughly 20% of the vibrating surface.

Both alloys samples were separated into different categories:

- The As-Machined (AM) samples: the samples were heat treated according to the pattern represented in Fig. 2a and were afterward machined to the wanted sample shape in Fig. 1.

- The Polished (P) samples: the samples were prepared as the As-Machined ones and then were polished with SiC papers from 500 to 4 000 grit.

- The SMATed-Aged (S+A) samples: the samples were machined to the wanted sample shape, they were then thermally treated according to the pattern in Fig. 2b, solution heat treatment followed by SMAT for a chosen duration and finally precipitation aging.

- The Aged-SMATed (A+S) samples: the samples were machined to the wanted sample shape, they were then thermally treated according to the pattern in Fig. 2c, solution heat treatment followed by precipitation aging and finally SMAT for a chosen duration.

The chosen heat treatments favor precipitation phenomena and were taken from an ASM handbook [33]. The number following the S in the sample denomination corresponds to the SMAT duration. For example, the 2024-S5+A sample was machined, then solution heat

105 treated at 495 °C for 1 h, SMATed during 5 min and precipitation aged at 190 °C for 10 h.
106 All successive steps of the thermo-mechanical treatments are detailed in Table 1. The SMAT
107 duration usually range from 1 to 30 min on flat samples in the literature. To avoid excessive
108 surface damage, the SMAT duration was limited at 10 min on the rotating samples. The
109 surface integrity and notch sensitivity are of primary importance in fatigue tests and will be
110 further discussed in the discussion section (4.2). The AM and P samples were both machined
111 after the thermal treatment to exhibit the impact on the fatigue resistances of a machined
112 surface compared to a polished one. The machining of S+A samples was executed before
113 the thermal treatments to avoid the formation of precipitates due to the heating of the tool
114 during this step if it occurred between the solution treatment and the SMAT as it would
115 alter the effect of the precipitation aging on the surface and the impact of SMAT. Addi-
116 tionally, the machining had to be made before SMAT to avoid altering the surface integrity
117 obtained by SMAT. The A+S samples followed the same pattern to allow the comparison
118 with the S+A samples.
119

120 *2.2. Characterization*

121 Microstructure observations were made, after polishing to mirror finish, on cross-section
122 samples cut perpendicularly to the longitudinal axis. Images were acquired by scanning
123 electron microscopy (SEM) with a ZEISS Supra 40 apparatus.

124 Microhardness profiles were measured on those cross-sections with a 25 g load. The
125 measurements were spaced by 30 μm and started at 30 μm below the surface. 15 profiles
126 were averaged and allowed to determine three characteristics: the core hardness, the sur-
127 face hardness enhancement relative to the core hardness and the affected depth where the
128 hardness dropped back to the core hardness.

129 Surface roughness was measured with a stylus surface profilometer on the 6 mm diameter
130 section with an average of 6 measurements.

131 Residual stress measurements were acquired with the XRD cosα method thanks to an
132 μ-X360 Pulstec apparatus with a chromium source [34]. The equipment was positioned

so that residual stresses were measured along the L direction. The residual stress profiles were obtained from measurements after successive electropolishing of the fatigue samples. Correction for the effect of surface removal on residual stress was performed according to Moore et al. [35] as the geometry of the pocket and samples allow it. A fit of the measured values was applied according to Curtis et al. [14]. A Proto Electropolisher Model 8818-V2 was used with the electrolytic solution (6% perchloric acid, 35% butoxyethanol and 59% methanol). The surface removal depth after each successive electropolishing was measured with a stylus surface profilometer. The Full Width at Half Maximum (FWHM) was extracted from each XRD profiles measured as an alternative way to measure the depth at which the process has influenced the microstructure. It is the width of the curve between two points positioned on each side of a diffraction peak at half of the maximum intensity.

Four points rotating bending fatigue tests were carried out at a rotating frequency of 30 Hz with an R. R. Moore test apparatus ($R = -1$). Samples were loaded to selected stress levels corresponding to fatigue lives between 10^5 and 2.10^6 cycles.

3. Results

3.1. Deformed structure analyses

Figs. 3 and 4 display the microstructures of 2024 and 7075, respectively. In each figure, both low and high magnification observations are given for the core microstructure and at the surface for S5+A and A+S5 treatments. The L direction is normal to the observed surfaces except for the Fig. 3e where it is vertical in the image.

In both alloys, large constituent phases were observed (up to 10 μm). They can be seen in Figs. 4a, b and c for the 7075. While they are also present in the 2024, they are not shown in the microstructures presented in Fig. 3. They were composed of insoluble intermetallic precipitates formed essentially during the alloys solidification. According to Wang et al. [36], this is due to the low solubility of Fe and Si in the aluminium alloys with Mg. Wang et al. also indicated that these precipitates tend to lower the damage resistance of the 2024

alloy while providing no strengthening. For the 7075-T651, Benedetti et al. [15] identified those intermetallic precipitates as $Cr_2Mg_3Al_{18}$ and $(Fe, Mn)Al_6$.

In the 2024, the low magnification core microstructure observation (Fig. 3a) highlights the high density of elongated intergranular Al_2Cu and Al_2CuMg phases formed during the heat treatment. These soluble intermetallic phases have a length of about 1 μm. They can be found with the names of θ and S phases in the literature as in the work of Zhang et al. [37]. These intergranular S phases should be differentiated from the intragranular S precipitates (also sometimes called S') formed during precipitation aging as Wang et al. highlighted [36]. Indeed, the intergranular S phases are coarser than the intragranular S precipitates. However, the Al_2Cu and Al_2CuMg phases cannot be differentiated simply from their size alone, as shown by Zhang et al. [37]. The higher magnification observation (Fig. 3d) presents the heterogeneous density of the intragranular T precipitates ($Al_{20}Cu_2Mn_3$ according to Wang et al.), they have a size lower than 100 nm when viewed from a transversal section. A major $\langle 111 \rangle$ fibre texture is known to develop along the extrusion direction (L direction) in aluminium alloys [32]. According to Wang et al., the S precipitates are needle and lath shaped, they are formed on $\{210\}_{Al}$ habit planes and are elongated along the $\langle 100 \rangle_{Al}$ direction. The angle between $\langle 111 \rangle$ and $\langle 100 \rangle$ direction is of about 55°. This description corresponds to the precipitates in Fig. 3e that were thus identified as S precipitates. Those precipitates have an angle of about 55° with the extrusion direction (vertical direction). The small size of the S precipitates and their orientation make it difficult to identify them in the other cross-section images. The use of SMAT generated important modifications in the microstructure, for both A+S and S+A samples. In Fig. 3b, the A+S5 treatment presents fragmented Al_2Cu and Al_2CuMg phases within the first 20 μm from the surface. Those phases show more spheroidal shapes within the extremely deformed region compared to the elongated shapes in the core areas, making it harder to identify the microstructure before SMAT. The density of the Al_2Cu and Al_2CuMg phases is also slightly lower at the surface for the A+S5 treatment as compared to the core microstructure. The Fig. 3f presents a higher heterogeneity coupled with a slightly lower density of the T precipitates at the surface of the A+S5 treated sample compared to the core material. In contrast, the

S5+A treatment (Fig. 3c) presents a higher overall Al_2Cu and Al_2CuMg phases density compared to the core microstructure and to the A+S5 samples. Those phases are also smaller and more homogeneously distributed within the nanostructured region compared to the A+S5 samples. Similarly to the A+S5 treatment, the S5+A treatment exposes a different morphology for Al_2Cu and Al_2CuMg phases within the first 20 μm with a favored spheroidal shape compared to the core morphology. The S5+A treatment also revealed a beginning of recrystallization with a pronounced restoration in Fig. 3g.

For the 7075, other than the intermetallic constituents, small plate-like $MgZn_2$ precipitates between 50 and 100 nm are visible in Fig. 4f, similar to the observations of Shaeri et al. [38]. They are mostly intragranular precipitates of high density and homogeneous distribution. For the A+S5 treatment (Fig. 4b), the large intermetallic precipitates remain at the surface, although some of them were broken during the high intensity SMAT. Two higher magnification observations of the SMATed region are presented, one just below the surface (Fig. 4d) and the second 30 μm below the surface (Fig. 4e). Fig. 4d displays the precipitation state within the nanostructured area. Precipitates can still be seen, however, with a significantly lower density, only the larger ones remain and they also appear slightly blurred. 30 μm below the surface (Fig. 4e), the $MgZn_2$ precipitates density is still lower than in the core regions. The precipitates are sharper compared to those closer to the surface and smaller ones can once again be seen. Differences between the A+S5 and S5+A treatments are not visible at the lower magnification (Fig. 4b and c, respectively). The Fig. 4g (S5+A) shows a restoration without recrystallization. According to Panigrahi et al., the recrystallization in highly deformed 7075 (true strain 2.3) begins at 150 °C, slightly above the aging temperature [39]. The 50 nm $MgZn_2$ precipitates are also present in lower density compared to the core region. However, a high density of homogeneous precipitates significantly smaller can barely be seen in the zoomed section of this same image. According to the literature, they correspond to η' precipitates [38]. Those precipitates should be present in the core images but their lower density prevent their detection.

3.2. Roughness

The surface roughness Ra and Rz characteristics are given for each surface condition in Table 2. Whatever the type of material, the AM and P surface roughness Rz values were similar about 5.8 μm and about 0.5 μm, respectively. For both materials, the Rz after the S+A treatments were always higher compared to that after A+S treatments by about +16% for the 2024 (31 μm to 36 μm) and by about +36% for the 7075 (25 μm to 34 μm). The increase in SMAT duration did not affect significantly the surface roughness parameters Ra and Rz for both treatments (A+S and S+A) and materials. The Ra parameter showed discrepancies between the A+S and S+A treatments proportional to those observed for the Rz.

3.3. Surface and subsurface properties

The evolution of the surface and sub-surface hardness has been investigated and follow the same evolution pattern for all treatments. The hardness, high at the surface, progressively decreases toward the core hardness as the depth from the surface increases. As the hardness measurements in the aluminium alloys display large discrepancies, a significant number of measurements were needed to reach a statistical reliability. Thus, instead of the superposing curves with high standard deviations, three characteristics were extracted and are presented in Table 2. These characteristics are the core hardness, the surface hardness enhancement and the affected depth. A curve in Table 2 highlights how the characteristics were measured. The core hardness is presented as a material characteristic as all samples of a given alloy underwent the same thermal treatment. The surface hardness enhancement is presented as the increase in percentage compared to the core hardness. The affected depth represents the minimum distance from the surface where the core hardness can be measured. On the 2024, the surface hardness after SMAT was similar for both S+A and A+S. Also, changes in SMAT duration did not affect significantly the A+S treated samples surface hardness nor their hardened depth. However, the affected depth increased by about 30% for the S+A treatments compared to the A+S ones. For the 7075, the S+A treatments values were lower than the A+S treatments ones. Only the S10+A barely compared to the

A+S5 treatment in terms of both surface hardness enhancement and affected depth. The affected depth and the surface hardness enhancement were affected by the SMAT duration. For S+A treatments, both were improved by 50% and 100% respectively while the A+S treatments have seen an enhancement only in the surface hardness by nearly 70%, with an increase in SMAT duration.

As an alternative way to quantify the depth at which the process has modified the microstructure, Fig. 5 presents the FWHM as a function of the depth for the 2024 (a) and the 7075 (b). Similar curves are visible for all treatments: high at the surface, the FWHM slowly decreases with the depth and eventually reaches a constant value. Results show very low discrepancies, providing a more accurate method than hardness to quantify process differences. Close to surface and for both alloys, the FWHM of A+S treatments are significantly higher than that of S+A treatments. It also appears that a longer SMAT duration only slightly increase the FWHM close to the surface. At 400 μm for the 2024 and at 300 μm for the 7075, the A+S treatments FWHM drops to a level comparable to the FWHM of S+A treatments. For both alloys, the FWHM of the A+S treatments reach a constant value at a depth of about 500 μm, this corresponds roughly to the affected depth by the hardness enhancement for these treatments (Table 2).

Residual stress profiles for the 2024 and 7075 alloys are represented in Figs. 6a and b, respectively. Each measured values of the S5+A, A+S5 and A+S10 2024 profiles (Fig. 6a) and the S5+A, S10+A and A+S5 7075 profiles (Fig. 6b) are individually indicated as a function of the depth. The surface residual stress is always in compression. At first the residual stress decreases, reaching the compression peak and afterward increases progressively. The residual stress eventually becomes positive, marking the beginning of the region in tension within the material. For both materials, the choice between the A+S and S+A treatments resulted in a significant stress profile modification while the impact of the SMAT duration was limited. The surface residual stress was reduced by 60% for both alloys for the S+A treatments compared to the A+S treatments. The compression peak intensity was also reduced by 30% for the 2024 and by 50% for the 7075 aluminium alloy. However, the S+A treatments displayed a peak position about 50% deeper in the subsurface compared to

the A+S treatments for both alloys. This resulted in a deeper compression region, in the S+A treatments, by 20% for the 2024 and 50% for the 7075. Interestingly, the 7075 always revealed higher residual stress compression levels compared to the 2024, for similar treatment conditions. For both alloys, the compressive residual stress intensity and the FWHM are both higher in the A+S treatments compared to the S+A treatments for similar depths.

For both alloys, residual stress measurements taken at the surface after fatigue tests exposed no sign of relaxation during the fatigue neither for A+S nor for S+A samples (not shown here).

3.4. Fatigue properties

Figs. 7a and b present the fatigue test results for the 2024 and 7075 alloys, respectively. Three tests were carried out for each surface condition. Each sample was tested at a given stress amplitude (y-axis) and ran either to fracture or to the run-out condition (over 10^6 cycles) for which the test was terminated. Either way, the number of cycles at which the test stopped is indicated on the x-axis. The run-out tests are indicated by arrows of the same colors, the arrow tail is positioned below the result at the same number of cycles than the corresponding run-out test.

For the 2024 (Fig. 7a), both the A+S5 (light blue hollow diamond) and A+S10 (dark blue diamond) treatment conditions provided fatigue resistances significantly higher (at least 25% higher at 10^6 cycles) than those recorded for the other surface treatments but close to each other. The SMAT duration did not appear to affect the fatigue resistance, in the range tested here. The lowest fatigue resistance is obtained for the As-Machined (hollow grey circle) surface. Both the S5+A (red square with a cross inside) and Polished (black circle) surface conditions displayed similar resistance levels only slightly higher than the AM condition.

For the 7075 (Fig. 7b), both the A+S5 and A+S10 treated surfaces provided with similar fatigue resistances that were only slightly higher than those of the Polished samples. For all the S+A conditions (red square markers) the fatigue properties were significantly worse

than the AM condition.

3.5. Post mortem fracture analyses

Fig. 8 gathers typical SEM fracture surface images of the AM, S5+A, A+S5, and A+S10 broken samples for the 2024 alloy. Dashed yellow lines represent fractographic features (river marks in particular) while white arrows show the fracture propagation direction. The fracture surface for the AM condition (Fig. 8a) shows clear river lines originating from a single initiation point (indicated by a red arrow) at the sample surface. The fracture initiated on a surface defect and propagated perpendicularly to the surface along circular arcs through the material. The fracture also initiated on surface defects for the S5+A (Fig. 8b) but several initiation sites were generally observed at the origin of the propagating crack. The A+S5 condition (Fig. 8d) displays the primary crack initiation sites in the subsurface. However, the A+S10 conditions (Fig. 8c and e) showed initiation sites either at the surface or in the subsurface. Figs. 8d and e both display primary crack initiation sites at a depth of about 300 μm (red arrows). In particular, shear lips can be seen between the initiation site and the surface for the A+S5, showing that the crack bridged to the surface only during the final fracture. For the A+S10 (Fig. 8e), a secondary crack (grey arrow) initiated from surface defects and propagated toward the center before quickly bridging to the primary crack.

Figs. 9a, b and d present the 7075 fracture surface SEM observations of AM, S5+A and S10+A samples, respectively. Figs. 9c and e are higher magnification images of the crack initiation regions for Fig. 9b and d. For all surface conditions, SEM observations revealed crack initiations on surface defects. For both the S5+A (Fig. 9b) and S10+A (Fig. 9d) treated samples, the cracks propagated mainly along the surface to a depth of around 1 mm before they deviated at an angle along a shear plane and propagated straight through the material. For the A+S treatment, SEM observations (not shown here) revealed small fatigue propagation areas before catastrophic propagation. The AM fracture surfaces did not show these characteristics and were similar to that of the 2024 AM samples (Fig. 8a).

4. Discussion

4.1. Modified microstructure

Severe plastic deformation by SMAT highly refined the microstructure and introduced high concentration of dislocations. For all the A+S conditions, when SMAT is carried out on a precipitation hardened microstructure, the high strain resulted in the dissolution of the smaller precipitates. This was attested by the lower density of fine precipitates in Figs. 3f and 4d for A+S conditions of the 2024 and 7075 alloys, respectively. In these locations, the larger precipitates were broken down into smaller ones and their shape changed from an elongated to a more spheroidal one. A similar mechanism was described by Straumal et al., they observed experimentally and showed theoretically how SPD increased the mobility of atoms which allowed the fragmentation and partial dissolution of precipitates in a Cu-3.9 at.% Ag as cast alloy [40]. However, when the precipitation treatment was carried out after SMAT (S+A treatments), a beginning of recrystallization for the 2024 and restoration for both alloys were observed in addition to a much higher density of precipitates.

Several authors in the literature revealed that a precipitation aging after severe plastic deformation yielded important benefits in terms of strength, ductility and hardness [20, 23, 24]. Those enhancements were attributed to smaller precipitates distributed more homogeneously. The dislocations introduced by deformation act as potential germination sites for the precipitates. The high density of such sites reduced the need for alloying elements diffusion and impaired precipitate growth. In the present work, the S+A treatments corresponding to this strategy indeed showed a high density of those small precipitates for the 7075. Similar precipitates should have been formed in the 2024 although the SEM resolution was insufficient to ascertain their presence. Three main parameters may influence the hardness in the treatments made: the dislocation density, the grain size and the precipitation. The FWHM measurements provided some insights on the first two parameters. Indeed, it describes the qualitative variations of dislocation densities and coherently diffracting domain sizes. Higher dislocation densities or smaller domains result both in a higher

FWHM. The importance of the recrystallization and dislocation recovery phenomena for the S+A treatments was highlighted as they resulted in a significant drop in FWHM.

For the 2024 alloy, despite the occurrence of these two phenomena, it is the high density of smaller precipitates in the S+A treatment that is responsible for the significant hardness enhancement of about 30%, comparable to the A+S treatments. From those observations, it can be concluded that the precipitates formed after SMAT produce higher hardness than the one formed by the same heat treatment without severe plastic deformation. Although the surface hardening for A+S and S+A treatments were comparable in the 2024 alloy, they did not originate from the same phenomena. According to literature, the S+A treatment increased precipitation hardening with lower dislocation densities and larger grain sizes should result in an improved ductility compared to the A+S treatment [20], which could confer some advantages for some industrial applications.

On the other hand, the S+A treatments are not as efficient in the case of the 7075. The 7075 S10+A treatment only yielded a surface hardness increase of about 13%, well below the 27% improvement of the A+S10 condition. For the 7075, the small precipitates formed appear less efficient at increasing the hardness than the SPD. This competition between softening induced by dislocation recovery and strengthening due to the precipitation phenomenon was also reported by Gutierrez-Urrutia et al. in a 6082 aluminium alloy after ECAP followed by aging [41]. Even though the 6XXX aluminium alloys have a strong potential for precipitation hardening, the strength of a SPDed 6082 dropped significantly after aging, mainly due to dislocation recovery.

The SMAT in S+A treatments was carried out on a softer material (after solution heat treatment) compared to that in A+S treatments. This resulted in significant differences between the S+A and A+S treatments and these differences dependent on the alloy. When applied on the 2024, S+A treatment is capable of generating a deeper affected layer than an A+S treatment (660 μm for S5+A versus 510 μm for A+S5, Table 2). For the 7075 alloy, the affected depths of the S+A conditions is lower (or comparable if the process time is doubled) than the A+S conditions (390 μm and 450 μm respectively for S5+A, S10+A treatments against 450 μm for both A+S5 and A+S10).

4.2. Effect on fatigue

The use of SMAT on soft surfaces (S+A treatments) resulted in high roughness indices and this is known to influence unfavorably the fatigue performance. Moreover, some benefices of SMAT were reduced by the aging treatment, such as compressive residual stresses which suffered a partial relaxation or the surface hardening which was reduced by recovery and recrystallization phenomena. All these elements result in a negative effect on the fatigue strength of the S+A treated samples. Although the aging also improved precipitation hardening which mitigated the impact of the recrystallization et recovery, especially in the 2024 alloy.

For 2024, even though the S+A treatments resulted in the deepest hardness enhancement coupled with the deepest compressive stress, the samples fatigue performances were not significantly different than the Polished (P) ones. This demonstrates that the high roughness values generated by these S+A treatments were compensated by the level of surface hardness and the compressive residual stress. When the SMAT was carried out after aging (A+S), the treated samples displayed a significant increase (about 25%) in stress levels for a failure at 10^6 cycles. Interestingly, the fatigue resistance obtained by the SMAT for the S+A treatment appeared far more stable against the residual stress relaxation compared to a conventional shot-peening treatment on an aged microstructure. Ludian & Wagner have run fatigue resistance tests similar to present work conditions on three types of precipitation aged 2024 (2024-T6) specimens: electropolished, shot-peened and shot-peened followed with a partial stress relaxation at 190 °C during 1 h (10 times shorter than the aging treatment used in the present work) [42]. The fatigue performance of their electropolished samples behaved similarly to the present Polished samples with a 200 MPa stress amplitude for 10^6 cycles to failure. The shot peened samples displayed a 225 MPa stress amplitude for 10^6 cycles to failure slightly lower than the A+S samples in the present work (250 MPa) even if their specimens had lower surface roughness than in the present work (Rz = 24 μm compared to Rz = 31 μm for A+S treatment or 36 μm for the S+A one). Even if their relaxation treatment is short, it was enough to provoke a 40% reduction in the stress leading to failure at 10^6 cycles, representing a 30% drop compared to the electropolished condition. In the

present work, S+A treated samples displayed a fatigue resistance comparable to Polished samples even though this condition has undergone a much longer relaxation treatment and has the highest surface roughness. This disparity in fatigue resistances between these two conditions tends to show that the compressive residual stresses induced by SMAT are more stable and are less affected by the relaxation than those introduced by shot-peening. When comparing the two SMATed conditions (A+S and S+A), the improved fatigue resistance of the A+S samples can be explained by the higher compressive residual stress at the surface coupled with a lower roughness. Both conditions have similar surface hardnesses, even though they are not of the same nature: the hardness in A+S samples is controlled by the grain size and the dislocation density whereas the hardness in S+A condition results mainly from the precipitation hardening. In both cases they should retard the local slip activity in the processed regions. The subsurface crack initiations observed in the A+S5 samples and their positions after the compressive residual stress peak revealed that the presence of significant compressive residual stresses prevent surface defects to generate large propagating cracks. At a relatively high stress level and despite a surface roughness significantly larger than after shot peening, no surface defects were activating long cracks for a targeted fatigue life of 10^6 cycles. While the A+S5 samples only showed subsurface crack initiations on grains having preferential orientations for slip activity, the A+S10 also displayed secondary crack initiations on surface defects. The parameters used to describe the surface roughness remained identical when increasing the processing time and may not be able to capture the occurrence of rare detrimental defects that could produce surface short cracks able to grow up to a large propagation stage. Further increase in SMAT duration might result in a negative effect on fatigue performance and an optimal SMAT processing time between 5 and 10 minutes is recommended in the present condition.

For the 7075, only the A+S treated samples maximizing the compressive surface residual stress, compression peak intensity and surface hardness displayed a fatigue resistance equivalent and eventually slightly above the Polished (P) samples. All other SMATed samples displayed extremely poor results compared to P samples and even to AM ones. Even with the help of high compressive residual stresses, the stress level for a failure at 10^6 cycles after

S+A treatments was significantly lower than for AM samples (about 15%). This illustrates how the 7075 alloy is sensitive to the presence of notches on its surface. The crack propagated along the surface rather than in the interior as displayed in Figs. 9b and d. The presence of multiple severe stress raisers at the sample surface facilitated the appearance of multiple cracks. They eventually bridged to form large cracks. Their propagations seem constrained at the surface by the presence of high compressive residual stresses. Finally, the crack that induced the sample failure has a lower penetration depth compared to AM or P samples as its shape increase significantly the stress intensity factor. Even with significant compressive residual stress, the defects introduced by SMAT on the surface highly impaired the high-cycle fatigue resistance of the processed part. As such, the high notch sensitivity of the 7075 makes it a poor choice of aluminium alloy for SMAT applications when trying to improve the fatigue resistance.

In terms of fatigue resistance, the effect of A+S versus S+A treatments were similar on both the 2024 and 7075 alloys: the A+S treatments perform better compared to the S+A treatments. The SMAT should be done after precipitation aging to maximize the fatigue resistance as the SPD hardness is comparable or even better than the hardness gain produced by S+A precipitation, the resulting compression residual stresses are higher, and the surface roughness values lower. SMAT had a superior potential for high-cycle fatigue resistance improvement on 2024 than on 7075. Indeed, the high notch sensitivity of the 7075 alloy makes it unsuited for fatigue resistance improvement with SMAT even if large compressive residual stress values can be obtained. On the other hand, the 2024 have shown conditions (A+S5 treatments) for which surface defects were not able to generate propagating cracks and nucleation happened at significantly higher stresses (+25%) than in the Polished condition. The level of compressive residual stress and the enhancement of hardness in the subsurface region was enough to prevent crack nucleation from the surface and the maximum potential seems to have been reached for this alloy as internal grains start to act as crack nucleation sites. Moreover, an increase in SMAT duration generated larger damage on the surface and sometimes resulted in crack nucleations from the surface. An optimal SMAT duration has to be found even if no significant impact on the fatigue

resistance was observed.

5. Conclusions

The results in this study showed that the fatigue behaviors of 2024 and 7075 aluminium alloys were influenced by the surface integrity after SMAT, the level of compressive residual stress and the precipitation aging coupled with SPD.

- The surface microstructure obtained by a precipitation aging after SMAT (S+A treatments) displayed finer and denser precipitates compared to both the core microstructure and the SMATed microstructure after precipitation aging (A+S treatments). However, since the SMAT was carried out on softer material, the surface integrity suffered as a higher roughness was generated along with fold-like defects, invisible to roughness measurements. Moreover, aging relaxed part of the introduced compressive residual stresses, lowering their intensity. The detrimental effects of the impaired surface integrity and the lower compressive residual stress intensity reduced the fatigue resistances of the S+A processed alloys. The fatigue resistances for Aged then SMATed (A+S) samples were always higher compared to SMATed then Aged (S+A) samples by about 25% for the 2024 and 20% for the 7075.

- For the 2024, S+A and Polished samples were comparable in terms of fatigue resistance and the A+S samples performed significantly better (+25% in terms of stress for failure at 10^6 cycles). However, the 7075 S+A treated samples showed a drop in fatigue resistance compared to both As-Machined and Polished samples while the 7075 A+S samples were barely better than Polished samples. The SMAT induced surface defects were extremely detrimental for the 7075 fatigue resistance due to the alloy high notch sensitivity. Thus, SMAT should be avoided on aluminium alloys with high notch sensitivity, especially when trying to improve the fatigue resistance.

- For both alloys, the SMAT duration parameter played a minor role on the residual stress profiles and on the fatigue resistance. However, it still displayed an importance

on the potential crack nucleation sites for the 2024. Increasing the duration from 5 to 10 min for the 2024 A+S treatments reduced the surface integrity as short crack initiated at the surface and were able to grow up to a large propagation stage.

- The S+A process was able to generate a microstructure more resistant to residual stress relaxation than the microstructure obtained after a conventional shot-peening on an aged material. In the case of the less notch sensitive alloy (2024), the resulting fatigue properties were equivalent to a Polished condition, showing that the level of compressive stress was enough to retard surface cracks nucleation even if the surface roughness was significant (Rz = 36 μm).

- The S+A process was also able to generate an impressive deep hardened layer on the 2024 with a depth 30% higher compared to the A+S treatments. That could be a manufacturing advantage for some industrial applications. The obtained S+A microstructures should also exhibit great ductility and tenacity than parts treated with the A+S treatment as a significant dislocation restoration process happens during aging.

Acknowledgements

The authors would like to acknowledge Dorian Delbergue and Dr. Marc Novelli for their valuable help, discussions and insights.

Funding: This work was supported by the French Government through the program "Investissements d'avenir" operated by the French National Research Agency (ANR) and referenced to as ANR-11-LABX-0008-01 ('LabEx DAMAS'). This work was also supported by the Laboratory of Optimization of Advanced Processes and Fabrication (LOPFA, Montréal, Canada).

References

[1] T. C. Lowe, R. Z. Valiev, The use of severe plastic deformation techniques in grain refinement, JOM Journal of the Minerals, Metals and Materials Society 56 (10) (2004) 64–68 (2004). doi:10.1007/s11837-004-0295-z.

[2] Y. Estrin, A. Vinogradov, Extreme grain refinement by severe plastic deformation: A wealth of challenging science, Acta Materialia 61 (3) (2013) 782–817 (2013). doi:10.1016/j.actamat.2012.10.038.

[3] I. A. Ovid'ko, R. Z. Valiev, Y. T. Zhu, Review on superior strength and enhanced ductility of metallic nanomaterials, Progress in Materials Science 94 (2018) 462–540 (2018). doi:10.1016/j.pmatsci.2018.02.002.

[4] K. Edalati, Z. Horita, A review on high-pressure torsion (HPT) from 1935 to 1988, Materials Science and Engineering: A 652 (2016) 325–352 (jan 2016). doi:10.1016/j.msea.2015.11.074.

[5] R. Z. Valiev, T. G. Langdon, Principles of equal-channel angular pressing as a processing tool for grain refinement, Progress in Materials Science 51 (7) (2006) 881–981 (sep 2006). arXiv:NIHMS150003, doi:10.1016/j.pmatsci.2006.02.003.

[6] C. S. Montross, T. Wei, L. Ye, G. Clark, Y. W. Mai, Laser shock processing and its effects on microstructure and properties of metal alloys: A review, International Journal of Fatigue 24 (10) (2002) 1021–1036 (2002). doi:10.1016/S0142-1123(02)00022-1.

[7] R. L. Murthy, B. Kotiveerachari, Burnishing of metallic surfaces - a review, Precision Engineering 3 (3) (1981) 172–179 (1981). doi:10.1016/0141-6359(81)90010-6.

[8] K. Lu, J. Lu, Nanostructured surface layer on metallic materials induced by surface mechanical attrition treatment, Materials Science and Engineering A 375-377 (1-2 SPEC. ISS.) (2004) 38–45 (2004). doi:10.1016/j.msea.2003.10.261.

[9] S. Bagheri, M. Guagliano, Review of shot peening processes to obtain nanocrystalline surfaces in metal alloys, Surface Engineering 25 (1) (2009) 3–14 (2009). doi:10.1179/026708408X334087.

[10] J. Azadmanjiri, C. C. Berndt, A. Kapoor, C. Wen, Development of Surface Nano-Crystallization in Alloys by Surface Mechanical Attrition Treatment (SMAT), Critical Reviews in Solid State and Materials Sciences 40 (3) (2015) 164–181 (2015). doi:10.1080/10408436.2014.978446.

[11] A. Heydari, R. Miresmaeili, S. Bagherifard, M. Guagliano, M. Aliofkhazraei, Incorporating the principles of shot peening for a better understanding of surface mechanical attrition treatment (SMAT) by simulations and experiments, Materials & Design 116 (2017) 365–373 (2017). doi:10.1016/j.matdes.2016.12.045.

[12] T. Grosdidier, M. Novelli, Recent Developments in the Application of Surface Mechanical Attrition Treatments for Improved Gradient Structures: Processing Parameters and Surface Reactivity, Materials Transactions 60 (7) (2019) 1344–1355 (jul 2019). doi:10.2320/matertrans.MF201929.

[13] V. Pandey, K. Chattopadhyay, N. C. Santhi Srinivas, V. Singh, Role of ultrasonic shot peening on low cycle fatigue behavior of 7075 aluminium alloy, International Journal of Fatigue 103 (2017) 426–435 (2017). doi:10.1016/j.ijfatigue.2017.06.033.

[14] S. Curtis, E. R. De Los Rios, C. A. Rodopoulos, A. Levers, Analysis of the effects of controlled shot peening on fatigue damage of high strength aluminium alloys, International Journal of Fatigue 25 (1) (2002) 59–66 (2002). doi:10.1016/S0142-1123(02)00049-X.

[15] M. Benedetti, V. Fontanari, P. Scardi, C. Ricardo, M. Bandini, Reverse bending fatigue of shot peened 7075-T651 aluminium alloy: The role of residual stress relaxation, International Journal of Fatigue 31 (8-9) (2009) 1225–1236 (aug 2009). doi:10.1016/j.ijfatigue.2008.11.017.

[16] H. Y. Miao, D. Demers, S. Larose, C. Perron, M. Lévesque, Experimental study of shot peening and stress peen forming, Journal of Materials Processing Technology 210 (15) (2010) 2089–2102 (2010). doi:10.1016/j.jmatprotec.2010.07.016.

[17] Y. Mutoh, G. H. Fair, B. Noble, R. B. Waterhouse, the Effect of Residual Stresses Induced By Shot-Peening on Fatigue Crack Propagation in Two High Strength Aluminium Alloys, Fatigue & Fracture of Engineering Materials & Structures 10 (4) (1987) 261–272 (1987). doi:10.1111/j.1460-2695.1987.tb00205.x.

[18] M. Novelli, J. J. Fundenberger, P. Bocher, T. Grosdidier, On the effectiveness of surface severe plastic deformation by shot peening at cryogenic temperature, Applied Surface Science 389 (2016) 1169–1174 (2016). doi:10.1016/j.apsusc.2016.08.009.

[19] M. Novelli, P. Bocher, T. Grosdidier, Effect of cryogenic temperatures and processing parameters on gradient-structure of a stainless steel treated by ultrasonic surface mechanical attrition treatment, Materials Characterization 139 (January) (2018) 197–207 (2018). doi:10.1016/j.matchar.2018.02.028.

[20] S. Cheng, Y. H. Zhao, Y. T. Zhu, E. Ma, Optimizing the strength and ductility of fine structured 2024 Al alloy by nano-precipitation, Acta Materialia 55 (17) (2007) 5822–5832 (2007). arXiv:9809069v1, doi:10.1016/j.actamat.2007.06.043.

[21] T. Hu, K. Ma, T. D. Topping, J. M. Schoenung, E. J. Lavernia, Precipitation phenomena in an ultrafine-grained Al alloy, Acta Materialia 61 (6) (2013) 2163–2178 (2013). doi:10.1016/j.actamat.2012.12.037.

[22] A. Dhal, S. K. Panigrahi, M. S. Shunmugam, Precipitation phenomena, thermal stability and grain growth kinetics in an ultra-fine grained Al 2014 alloy after annealing treatment, Journal of Alloys and Compounds 649 (2015) 229–238 (2015). doi:10.1016/j.jallcom.2015.07.098.

[23] Y. Chen, N. Gao, G. Sha, S. P. Ringer, M. J. Starink, Microstructural evolution, strengthening and thermal stability of an ultrafine-grained Al-Cu-Mg alloy, Acta Materialia 109 (2016) 202–212 (2016). doi:10.1016/j.actamat.2016.02.050.

[24] A. Kumar Singh, S. Ghosh, S. Mula, Simultaneous improvement of strength, ductility and corrosion re-

sistance of Al2024 alloy processed by cryoforging followed by ageing, Materials Science and Engineering A 651 (2016) 774–785 (2016). doi:10.1016/j.msea.2015.11.032.

[25] W. T. Huo, J. T. Shi, L. G. Hou, J. S. Zhang, An improved thermo-mechanical treatment of high-strength Al–Zn–Mg–Cu alloy for effective grain refinement and ductility modification, Journal of Materials Processing Technology 239 (2017) 303–314 (2017). doi:10.1016/j.jmatprotec.2016.08.027.

[26] SONATS Europe Technologies Group. (2020, April, 3).
URL https://sonats-et.com/en/shot-peening/what-is-shot-peening/

[27] H. W. Chang, P. M. Kelly, Y. N. Shi, M. X. Zhang, Thermal stability of nanocrystallized surface produced by surface mechanical attrition treatment in aluminum alloys, Surface and Coatings Technology 206 (19-20) (2012) 3970–3980 (2012). doi:10.1016/j.surfcoat.2012.03.069.

[28] Y. Liu, B. Jin, J. Lu, Mechanical properties and thermal stability of nanocrystallized pure aluminum produced by surface mechanical attrition treatment, Materials Science and Engineering A 636 (2015) 446–451 (2015). doi:10.1016/j.msea.2015.03.068.

[29] L. Wen, Y. Wang, Y. Zhou, L. Guo, J. H. Ouyang, Microstructure and corrosion resistance of modified 2024 Al alloy using surface mechanical attrition treatment combined with microarc oxidation process, Corrosion Science 53 (1) (2011) 473–480 (2011). doi:10.1016/j.corsci.2010.09.061.

[30] K. R. Lehr, H. Liu, Fatigue crack propagation and strain cycling properties, International Journal of Fracture Mechanics 5 (1) (1969) 45–55 (mar 1969). doi:10.1007/BF00189938.

[31] X. Huang, M. Torgeir, W. Cui, An engineering model of fatigue crack growth under variable amplitude loading, International Journal of Fatigue 30 (1) (2008) 2–10 (jan 2008). doi:10.1016/j.ijfatigue.2007.03.004.

[32] T. Grosdidier, P. Keramidas, J. J. Fundenberger, F. Wagner, P. Tsakiropoulos, Influence of atomised powder characteristics on texture and microstructure development in extruded Al-8Fe-4Ni base alloys 267 (1999) 71–81 (1999). doi:10.1016/S0921-5093(99)00063-5.

[33] G. Totten, Asm handbook volume 4e: Heat treating of nonferrous alloys, ASM International, USA (2016).

[34] PULSTEC INDUSTRIAL CO.,LTD (2020, April, 3).
URL https://www.pulstec.co.jp/en/product/x-ray/

[35] M. Moore, W. Evans, Mathematical correction for stress in removed layers in x-ray diffraction residual stress analysis, Tech. rep., SAE Technical Paper (1958).

[36] S. C. Wang, M. J. Starink, Precipitates and intermetallic phases in precipitation hardening Al–Cu–Mg–(Li) based alloys, International Materials Reviews 50 (4) (2005) 193–215 (2005). doi:10.1179/174328005X14357.

[37] X. Zhang, T. Hashimoto, J. Lindsay, X. Zhou, Investigation of the de-alloying behaviour of

625 θ-phase (Al2Cu) in AA2024-T351 aluminium alloy, Corrosion Science 108 (2016) 85–93 (2016).
626 doi:10.1016/j.corsci.2016.03.003.
627 [38] M. H. Shaeri, M. Shaeri, M. Ebrahimi, M. T. Salehi, S. H. Seyyedein, Effect of ECAP temperature on
628 microstructure and mechanical properties of Al-Zn-Mg-Cu alloy, Progress in Natural Science: Materials
629 International 26 (2) (2016) 182–191 (2016). doi:10.1016/j.pnsc.2016.03.003.
630 [39] S. K. Panigrahi, R. Jayaganthan, Effect of annealing on thermal stability, precipitate evolution, and
631 mechanical properties of cryorolled Al 7075 alloy, Metallurgical and Materials Transactions A: Physical
632 Metallurgy and Materials Science 42 (10) (2011) 3208–3217 (2011). doi:10.1007/s11661-011-0723-y.
633 [40] B. B. Straumal, V. Pontikis, A. R. Kilmametov, A. A. Mazilkin, S. V. Dobatkin, B. Baretzky, Competi-
634 tion between precipitation and dissolution in Cu–Ag alloys under high pressure torsion, Acta Materialia
635 122 (2017) 60–71 (2017). doi:10.1016/j.actamat.2016.09.024.
636 [41] I. Gutierrez-Urrutia, M. A. Muñoz-Morris, D. G. Morris, Recovery of deformation substructure
637 and coarsening of particles on annealing severely plastically deformed Al-Mg-Si alloy and anal-
638 ysis of strengthening mechanisms, Journal of Materials Research 21 (2) (2006) 329–342 (2006).
639 doi:10.1557/jmr.2006.0063.
640 [42] T. Ludian, L. Wagner, Effect of age-hardening conditions on high-cycle fatigue performance of me-
641 chanically surface treated Al 2024, Materials Science and Engineering: A 468-470 (SPEC. ISS.) (2007)
642 210–213 (nov 2007). doi:10.1016/j.msea.2006.07.169.

Treatment name	Step 1	Step 2	Step 3	Step 4
2024 As-Machined (AM)	495 °C - 1 h - WQ	190 °C - 10 h - AC	Machined	
2024 Polished (P)	495 °C - 1 h - WQ	190 °C - 10 h - AC	Machined	Polished
2024 SMATed5-Aged (S5+A)	Machined	495 °C - 1 h - WQ	SMATed - 5 min	190 °C - 10 h - AC
2024 Aged-SMATed5 (A+S5)	Machined	495 °C - 1 h - WQ	190 °C - 10 h - AC	SMATed - 5 min
2024 Aged-SMATed10 (A+S10)	Machined	495 °C - 1 h - WQ	190 °C - 10 h - AC	SMATed - 10 min
7075 As-Machined (AM)	465 °C - 1 h - WQ	122 °C - 24 h - AC	Machined	
7075 Polished (P)	465 °C - 1 h - WQ	122 °C - 24 h - AC	Machined	Polished
7075 SMATed3-Aged (S3+A)	Machined	465 °C - 1 h - WQ	SMATed - 3 min	122 °C - 24 h - AC
7075 SMATed5-Aged (S5+A)	Machined	465 °C - 1 h - WQ	SMATed - 5 min	122 °C - 24 h - AC
7075 SMATed10-Aged (S10+A)	Machined	465 °C - 1 h - WQ	SMATed - 10 min	122 °C - 24 h - AC
7075 Aged-SMATed5 (A+S5)	Machined	465 °C - 1 h - WQ	122 °C - 24 h - AC	SMATed - 5 min
7075 Aged-SMATed10 (A+S10)	Machined	465 °C - 1 h - WQ	122 °C - 24 h - AC	SMATed - 10 min

Table 1: Summary of successive thermo-mechanical treatment steps for each sample condition studied.

Material	Treatment	Ra (μm)	Rz (μm)	Surface Hardness Enhancement	Affected depth (μm) $\pm$ 30 μm (stepsize)
2024	AM	1.00 ± 0.10	5.81 ± 0.55	None	None
Core hardness	P	0.07 ± 0.02	0.42 ± 0.11		
119 $HV_{0.5} \pm 6$	S5+A	7.17 ± 0.78	36.48 ± 3.65	$+30\% \pm 9\%$	660
	A+S5	5.99 ± 0.63	30.41 ± 2.25	$+28\% \pm 6\%$	510
	A+S10	6.08 ± 0.57	31.92 ± 3.18	$+33\% \pm 9\%$	510
7075	AM	1.01 ± 0.09	5.86 ± 0.67	None	None
Core hardness	P	0.09 ± 0.01	0.60 ± 0.10		
154 $HV_{0.5} \pm 7$	S3+A	6.67 ± 0.47	35.31 ± 2.04	$+6\% \pm 2\%$	300
	S5+A	6.77 ± 0.68	34.81 ± 3.05	$+10\% \pm 5\%$	390
	S10+A	6.35 ± 0.53	32.73 ± 2.57	$+13\% \pm 3\%$	450
	A+S5	4.66 ± 0.42	24.38 ± 2.10	$+16\% \pm 5\%$	450
	A+S10	4.92 ± 0.31	25.80 ± 2.03	$+27\% \pm 9\%$	450

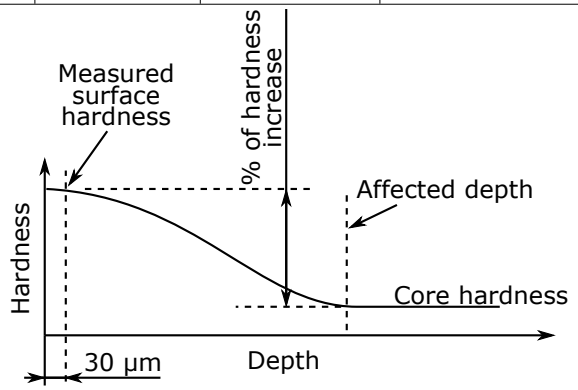

Table 2: Roughness Ra (μm) and Rz (μm) parameters are given for both materials and all treatments. The initial hardness ($HV_{0.5}$) is given for both materials, the surface hardness relative increase and the affected depth is given for all treatments on both materials. A common hardness curve evolution as a function of the depth is represented at the bottom of the table with the locations where the characteristics were measured.

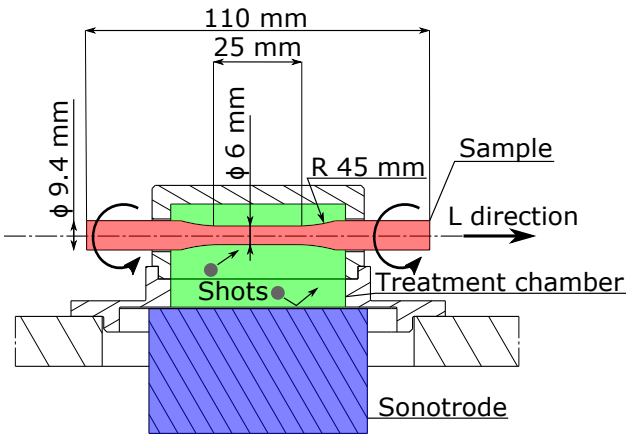

Figure 1: Representation of the Surface Mechanical Attrition Treatment (SMAT) on cylindric samples. The sample is shown in red, the treatment chamber where the media is located is in green and the vibrating part (sonotrode) propelling the spherical shots is in blue.

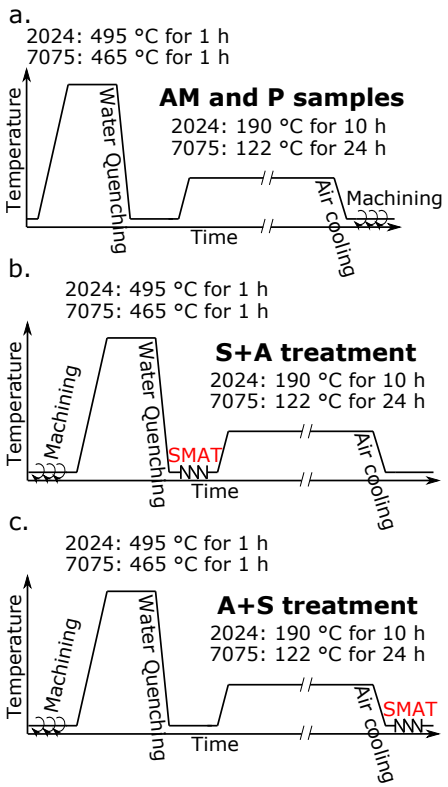

Figure 2: Thermal treatment for the As-Machined (AM) and Polished (P) samples (a) along with thermo-mechanical treatments for the S+A (b) and A+S (c) samples.

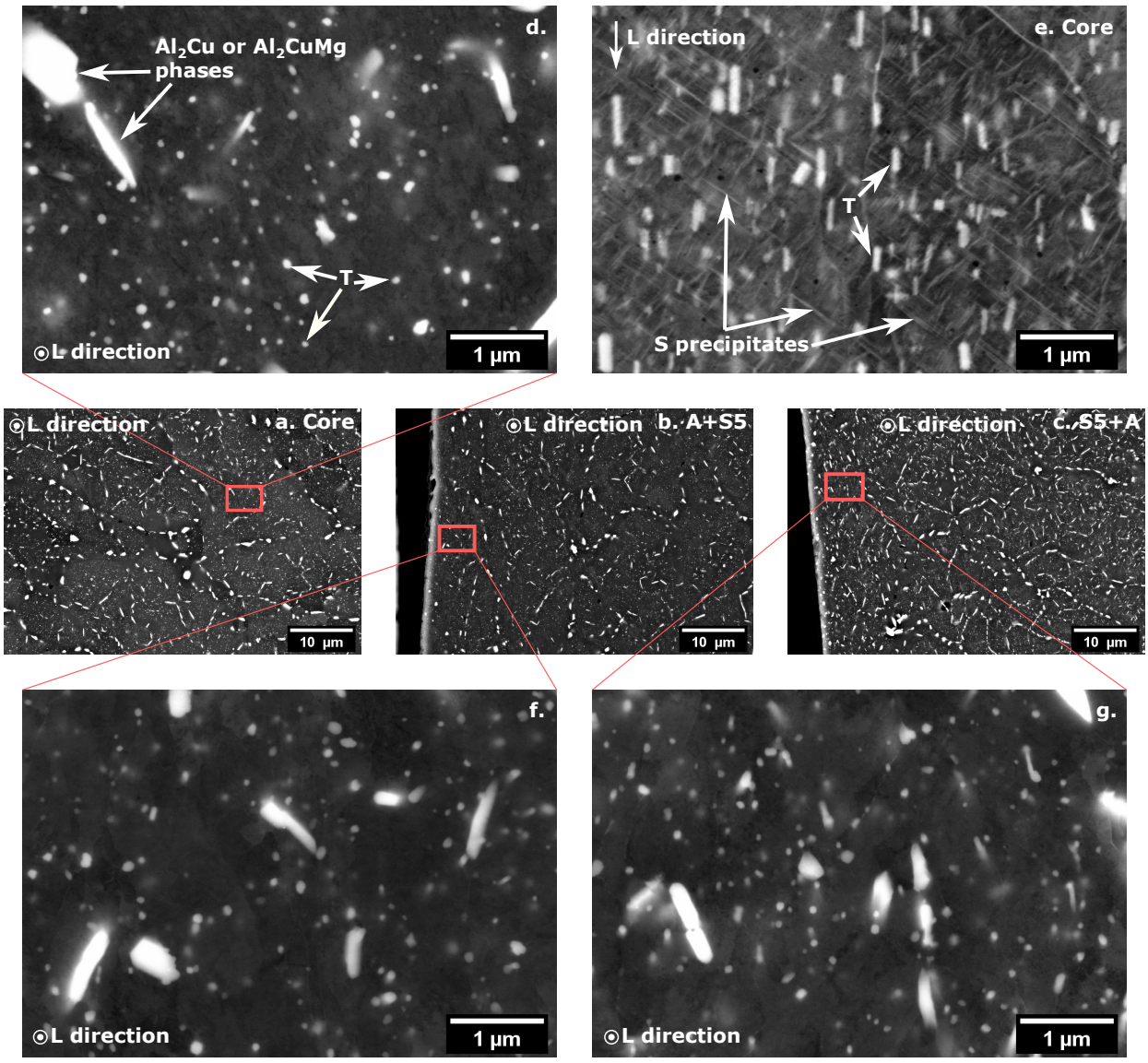

Figure 3: SEM observations of the 2024 cross-sections. The core microstructure is shown (a, d and e), the surface microstructures after A+S5 and S5+A treatments are respectively in the images b, f and c, g. A low magnification (a, b, c) and higher magnification (d, f, g) are presented for each condition. The e microstructure observation was parallel to the L direction.

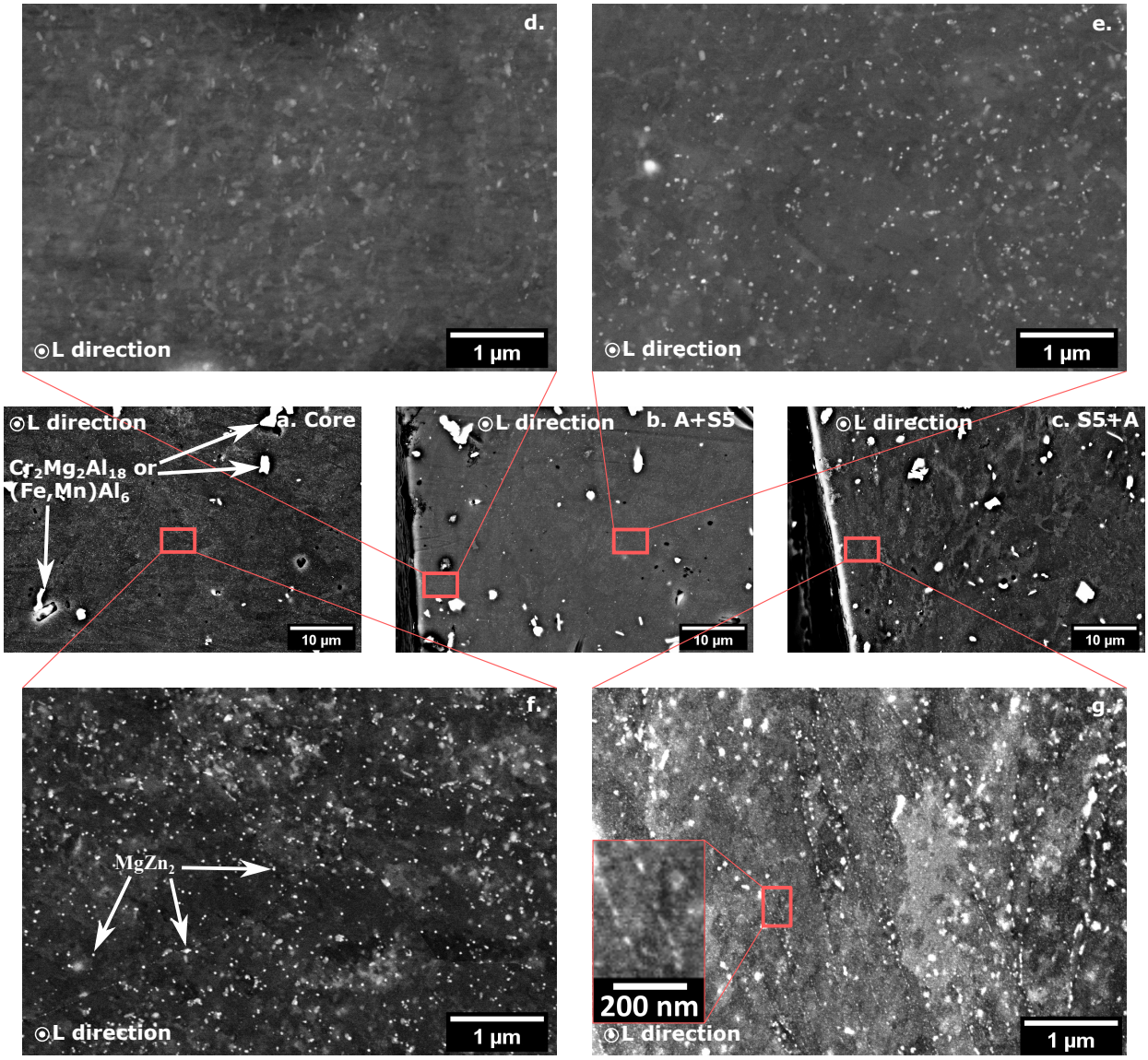

Figure 4: SEM observations of the 7075 cross-sections. The core microstructure is shown (a, f), the surface microstructure after A+S5 and S5+A treatments are respectively in the images b, d, e and c, g. Low magnifications (a, b, c) and higher magnifications (d, e, f, g) images are presented for each condition.

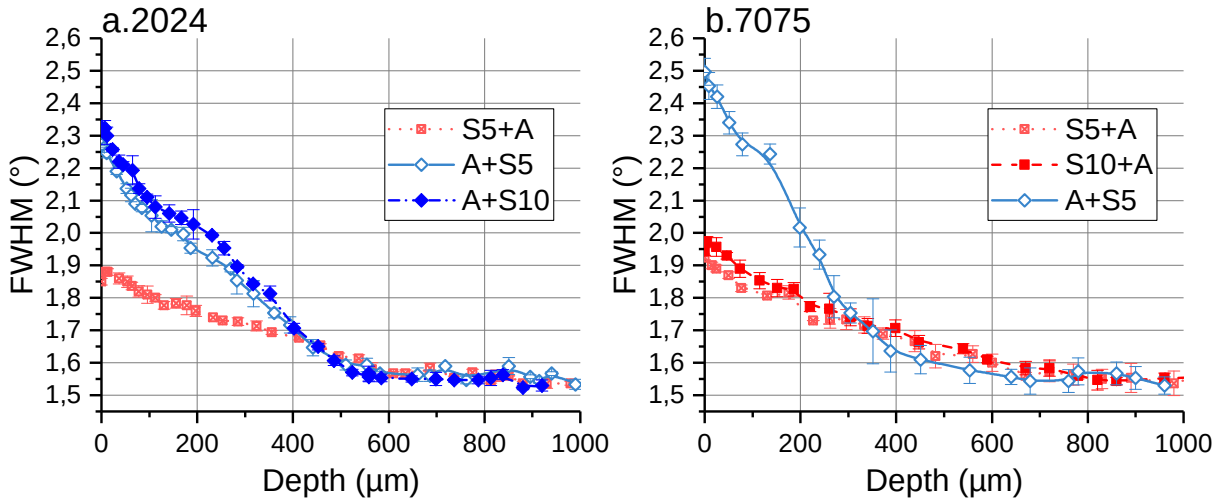

Figure 5: Full Width at Half Maximum (FWHM) as a function of the depth for 2024 (a) and 7075 (b).

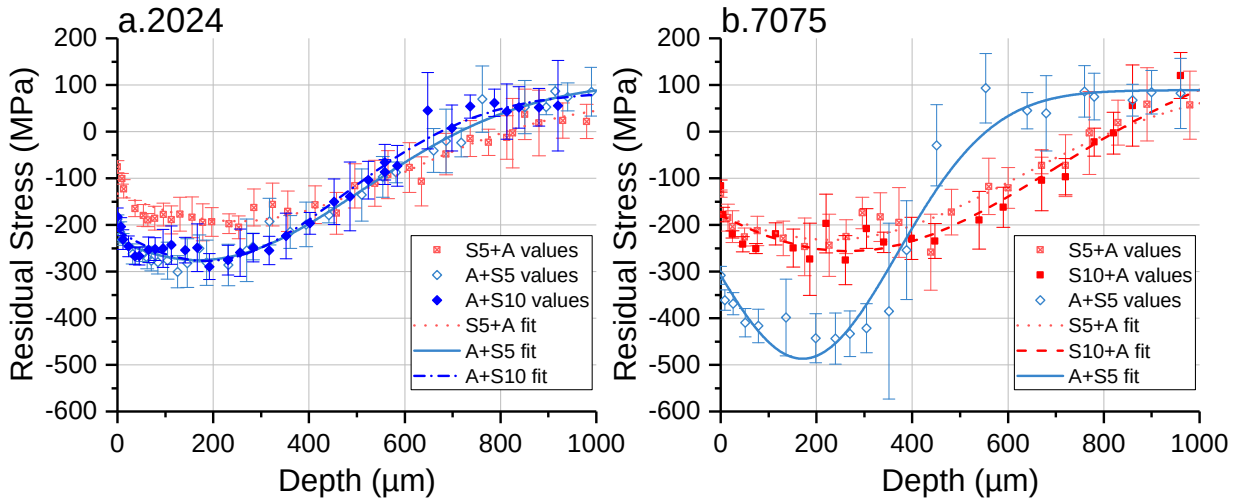

Figure 6: Residual stress profiles for different treatments on both materials. The residual stress values and corresponding fits are shown. The S5+A, A+S5 and A+S10 treatments are evaluated for the 2024 (a) and the S5+A, S10+A and A+S5 treatments are evaluated for the 7075 (b).

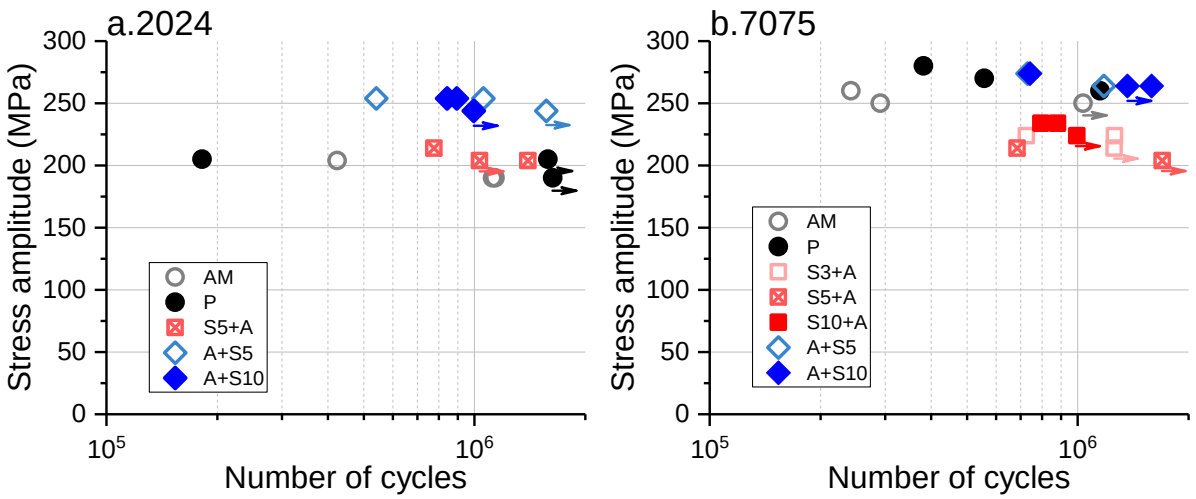

Figure 7: Stress and number of cycles to failure for different treatments on the 2024 (a) and 7075 (b).

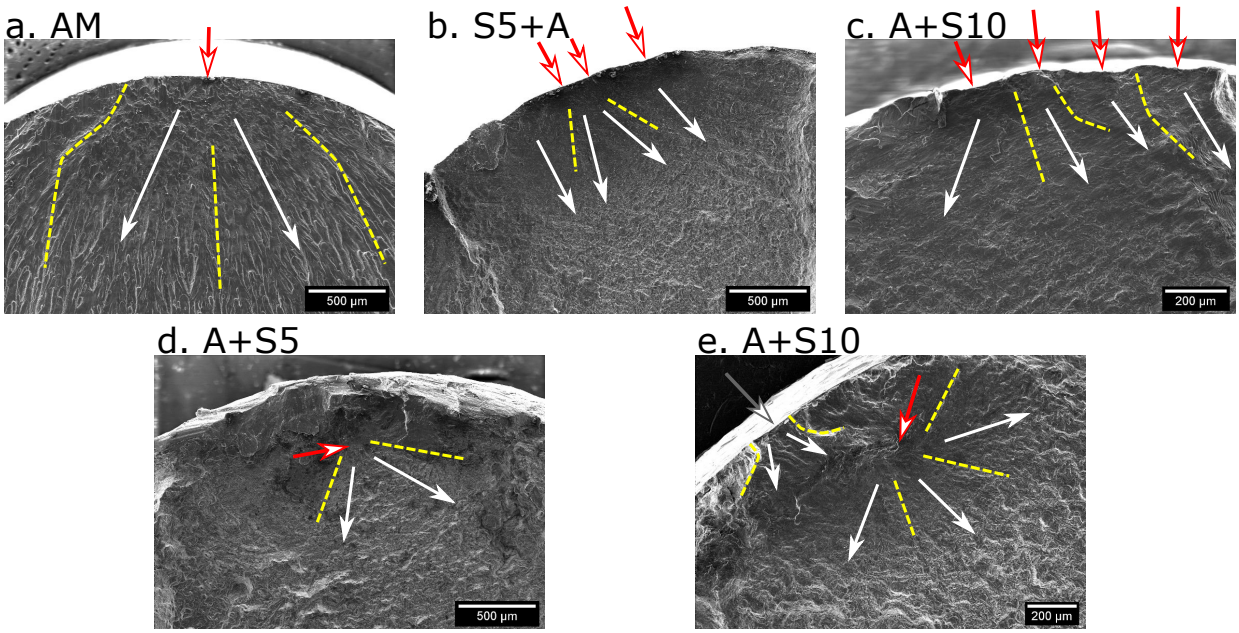

Figure 8: Fracture surface observed by SEM for AM (a, 424 000 cycles at 204 MPa), S5+A (b, 776 000 cycles at 214 MPa), A+S5 (d, 1 058 000 cycles at 214 MPa) and A+S10 (c, 895 000 cycles at 254 MPa and e, 843 000 cycles at 254 MPa) treatments on 2024.

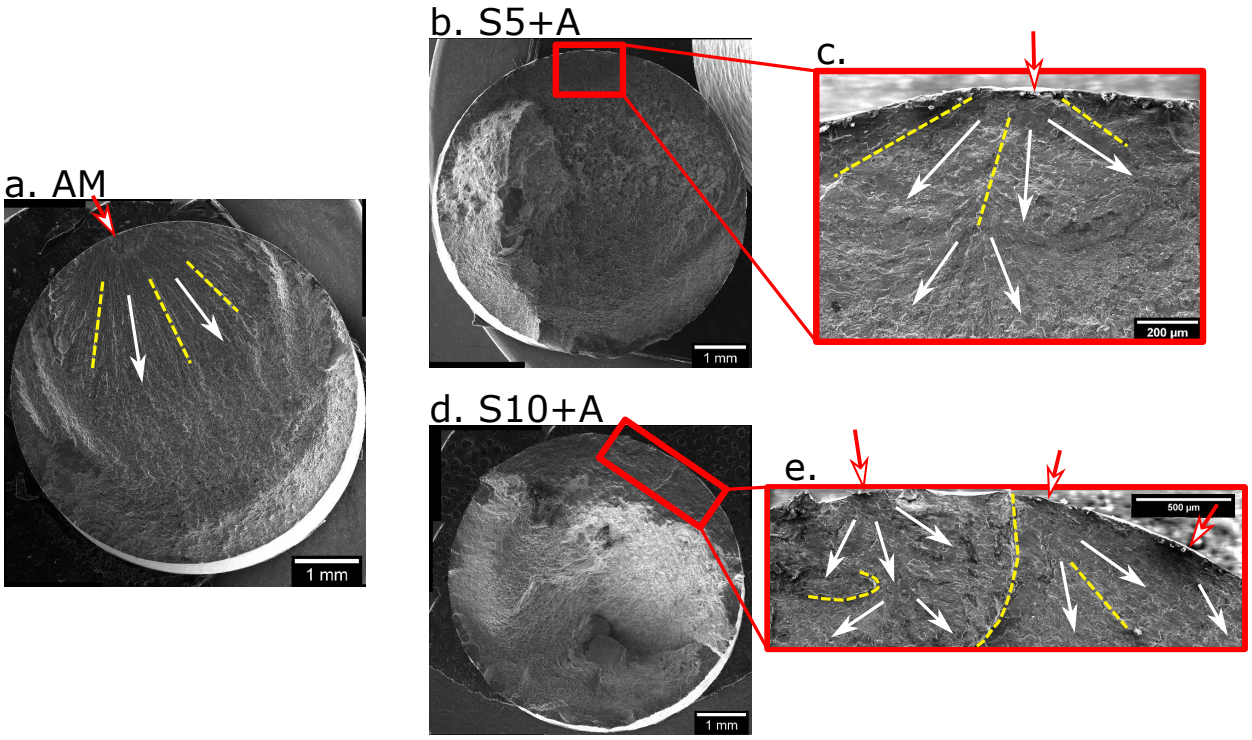

Figure 9: Fracture surface images by SEM for AM (a, 291 000 cycles at 250 MPa), S5+A (b, 684 000 cycles at 214 MPa) and S10+A (d, 881 000 cycles at 234 MPa) treatments on 7075. Higher magnification images on the primary crack initiation location are shown in c and e for S5+A and S10+A treatments, respectively.